




Cite this: *J. Mater. Chem. C*, 2022, 10, 5550

## Stable and wide-wavelength tunable luminescence of CsPbX<sub>3</sub> nanocrystals encapsulated in metal–organic frameworks†

Hailong Wu, Lijia Yao, Wenqian Cao, Yu Yang,  Yuanjing Cui,  \* Deren Yang  and Guodong Qian  \*

Lead-halide perovskite nanocrystals (PeNCs) possess attractive linear and nonlinear optical properties. However, further adjusting their linear and nonlinear optical properties in a facile way remains a great challenge due to the inevitable instabilities. Herein, an effective host–guest system was successfully constructed by encapsulating PeNCs (CsPbX<sub>3</sub> NCs) into a metal–organic framework (MOF), ZJU-28, via a sequential deposition method at ambient conditions. The accessible and charged frameworks of ZJU-28 facilitate the confinement growth of CsPbX<sub>3</sub> NCs in the channels under a mild environment, and therefore facile halide-composition adjustment can be achieved by simply tuning the halide stoichiometry of CsX in a solution process, enabling wide-wavelength tunable one- and two-photon excited (1PE and 2PE) luminescence from 450 nm to 660 nm. Moreover, besides the confinement effect, effective separation, passivation and protection of CsPbX<sub>3</sub> NCs are still achieved in ZJU-28⊃CsPbX<sub>3</sub> crystals, resulting in a giant two-photon action cross-section which is comparable to that of colloidal CsPbX<sub>3</sub> NCs densely capped by surface ligands, and significantly enhanced 1PE and 2PE photostability especially for the spectral stability of mixed-halide composites. These results will pave the way for the exploitation of highly stable and emission-tunable PeNCs composites in optoelectronic applications and even future integrated photonics.

Received 7th January 2022,  
Accepted 2nd March 2022

DOI: 10.1039/d2tc00075j

rsc.li/materials-c

## Introduction

Lead-halide perovskite nanocrystals (PeNCs) have been widely recognized as emerging luminescent materials and promising candidates in the fields of display backlights, light emitting diodes (LEDs), lasers and photodetectors due to the combination of a high photoluminescence quantum yield (PLQY), large absorption coefficient, high color purity and tunable bandgap.<sup>1–6</sup> Besides the exceptional linear optical characteristics, PeNCs still exhibit superior nonlinear optical properties especially for two-photon absorption (2PA) compared with traditional semiconductor nanocrystals and organic molecules, which further broaden their applications benefited from longer wavelength absorption.<sup>7–9</sup> Many efforts have been devoted to exploring the relationship between the nonlinear absorption capacity and the sizes, shape and also the composition of PeNCs, aiming at promoting and tuning their nonlinear

optical properties.<sup>10–12</sup> Compositional engineering such as halogen substitution is an effective way to adjust the electronic structure and bandgap of PeNCs, thereby further optimizing their nonlinear absorption capacity to enable full visible spectrum modulation of up-conversion luminescence.<sup>13,14</sup> However, PeNCs are vulnerable to light, oxygen, heat, moisture and polar solvent and are severely degraded under ambient conditions due to their inherent ionic nature and low formation energy.<sup>15</sup> In particular, iodine-containing PeNCs are more volatile because large-radius iodide ions in the perovskite lattice lead to a lower Goldschmidt tolerance factor (below 0.9), which indicates their intrinsic structural instability under ambient conditions.<sup>16</sup> These iodine-containing PeNCs also exhibit poor phase stability and tend to spontaneously undergo phase transition into the undesired non-luminous phase once they are exposed to prolonged illumination, humidity or high temperature.<sup>17,18</sup> Furthermore, some mixed-halide PeNCs show compositional instability in the form of the migration of halide ions and the segregation of halides into separate iodide- and bromide-rich domains under illumination or applied bias, which leads to localized variations in the material band gap and adversely impacts the emission spectrum and color.<sup>19–21</sup> Although the isolation and passivation effect enabled by

State Key Laboratory of Silicon Materials, Cyrus Tang Center for Sensor Materials and Applications, School of Materials Science and Engineering, Zhejiang University, Hangzhou 310027, China. E-mail: cuiyj@zju.edu.cn, gdqian@zju.edu.cn

† Electronic supplementary information (ESI) available: The synthesis and supplementary figures and table of the characterization of the as-prepared materials. See DOI: 10.1039/d2tc00075j

anchoring PeNCs on the surface of silica spheres, or embedding PeNCs into stable hosts such as polymers, inorganic salts, SiO<sub>2</sub>, glass and zeolites, can alleviate the stability issues, the research subjects mainly focus on CsPbBr<sub>3</sub> NCs, one of the most stable species of PeNCs.<sup>22–27</sup> More efforts are needed to stabilize mix-halide PeNCs and those containing iodine. Therefore, it remains a great challenge to stabilize PeNCs and further optimize and tune their nonlinear optical properties *via* compositional engineering.

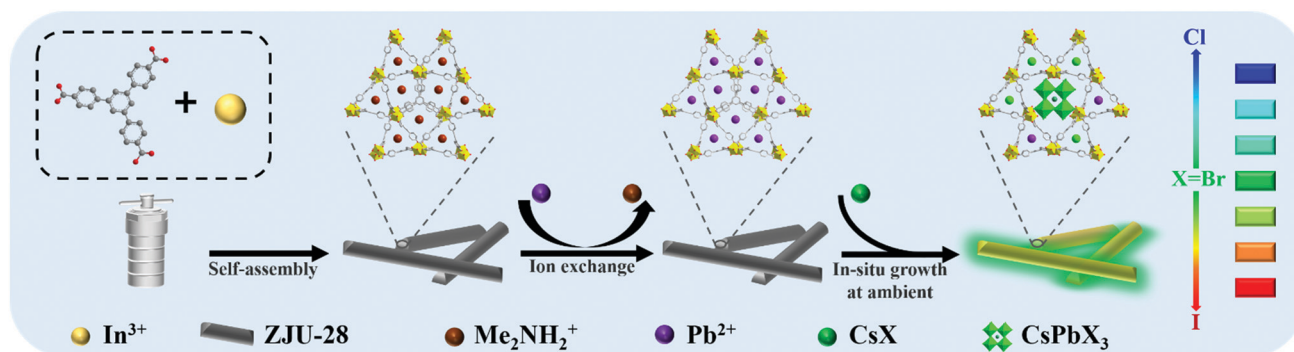
Host–guest systems constructed by encapsulating PeNCs into host materials with specific methods are usually utilized to address the above issues. CsPbX<sub>3</sub> NCs have been successfully stabilized in glass *via* a conventional melt-quenching technique, or in zeolites *via* a modified hot-injection method, both of which enable full spectrum adjustment of up-conversion luminescence.<sup>28,29</sup> However, the ultrahigh temperature is indispensable in the melt-quenching technique and tedious conditions such as heating and a nitrogen atmosphere are highly required in the hot-injection method. Recent intriguing porous materials, metal–organic frameworks (MOFs), have been demonstrated to be multifunctional platforms for the successful incorporation of dye molecules, carbon dots and even nanoparticles, owing to their high porosity, tunable pores/channels and specific sites.<sup>30–33</sup> The accessible and charged frameworks (*e.g.* anionic MOF, ZJU-28) enable enrichment of the constituent elements of perovskites (lead and caesium) *via* ion exchange processes in solution and trigger nucleation and growth of PeNCs inside hydrophobic pores/channels of MOFs under an ambient environment.<sup>34,35</sup> In addition, this ion exchange process in synthetic procedures offers great convenience for compositional engineering of the *in situ* formation of PeNCs under mild conditions. Therefore, the combination of PeNCs and MOFs seems to be a facile and effective strategy to simultaneously stabilize PeNCs and tune their nonlinear optical properties.

Herein, host–guest ZJU-28⊃CsPbX<sub>3</sub> was constructed by encapsulating CsPbX<sub>3</sub> NCs into an anionic MOF, ZJU-28 (ZJU-28 = [In<sub>3</sub>(BTB)<sub>4</sub>](Me<sub>2</sub>NH<sub>2</sub>)<sub>3</sub>), *via* a novel sequential deposition approach, during which *in situ* growth of CsPbX<sub>3</sub> NCs was realized by sequentially depositing Pb<sup>2+</sup> and CsX into the channels of ZJU-28. The whole growth process of CsPbX<sub>3</sub> NCs was carried out under mild conditions and their halide

composition can be simply tuned from Cl<sub>2</sub>Br to BrI<sub>2</sub> by adjusting the halide stoichiometry of CsX during the second deposition process, resulting in successfully tuning the 1PE and 2PE luminescence of ZJU-28⊃CsPbX<sub>3</sub> crystals covering almost the full-vision region. Thanks to the strong confinement and surface passivation provided by ZJU-28 frameworks, ZJU-28⊃CsPbX<sub>3</sub> crystals exhibit a giant two-photo action cross-section (8.66 × 10<sup>4</sup> GM for ZJU-28⊃CsPbClBr<sub>2</sub> at 780 nm, 1.58 × 10<sup>6</sup> GM for ZJU-28⊃CsPbBr<sub>3</sub> at 780 nm and 1.96 × 10<sup>5</sup> GM for ZJU-28⊃CsPbBrI<sub>2</sub> at 980 nm, respectively), which is comparable to that of colloidal CsPbX<sub>3</sub> NCs dispersed in toluene. Moreover, ZJU-28 frameworks also separate and passivate the internal CsPbX<sub>3</sub> NCs, resulting in significantly enhanced 1PE and 2PE photostability especially for the spectral stability of mixed-halide composites.

## Results and discussion

Anionic MOF ZJU-28 was chosen as the host to encapsulate CsPbX<sub>3</sub> NCs and ZJU-28⊃CsPbX<sub>3</sub> crystals were synthesized *via* a sequential deposition method at ambient conditions, as shown in Scheme 1. Firstly, lead ions were introduced into the channels of ZJU-28 by replacing the dimethylamine cations (Me<sub>2</sub>NH<sub>2</sub><sup>+</sup>) to form ZJU-28⊃Pb<sup>2+</sup> crystals.<sup>36</sup> The obtained ZJU-28⊃Pb<sup>2+</sup> crystals were then impregnated into a methanol solution of CsX to trigger the *in situ* growth of CsPbX<sub>3</sub> NCs within ZJU-28. It is worth noting that the CsX solution provides all the halogens in this reaction, therefore, a series of ZJU-28⊃CsPbX<sub>3</sub> crystals was successfully synthesized by simply adjusting the halide stoichiometry of CsX from Br to Cl/Br or Br/I, including ZJU-28⊃CsPbCl<sub>2</sub>Br, ZJU-28⊃CsPbCl<sub>1.5</sub>Br<sub>1.5</sub>, ZJU-28⊃CsPbClBr<sub>2</sub>, ZJU-28⊃CsPbBr<sub>3</sub>, ZJU-28⊃CsPbBr<sub>2</sub>I, ZJU-28⊃CsPbBr<sub>1.5</sub>I<sub>1.5</sub>, and ZJU-28⊃CsPbBrI<sub>2</sub>. All experiments were carried out under an ambient environment without any atmosphere protection, which makes the in-situ formation and composition regulation of CsPbX<sub>3</sub> NCs facile. The various colors of the acquired samples and their blue to red emission under UV light are indicative of the successful formation of CsPbX<sub>3</sub> NCs with different halide compositions in ZJU-28 (Fig. S1, ESI<sup>†</sup>). As a comparison, a series of colloidal CsPbX<sub>3</sub> NCs (X<sub>3</sub> = Cl<sub>2</sub>Br, Cl<sub>1.5</sub>Br<sub>1.5</sub>, ClBr<sub>2</sub>, Br<sub>3</sub>, Br<sub>2</sub>I, Br<sub>1.5</sub>I<sub>1.5</sub>, BrI<sub>2</sub>) was also prepared *via* a typical hot-injection method (Fig. S2, ESI<sup>†</sup>).<sup>13</sup>



Scheme 1 Schematic diagram of the *in situ* synthesis of ZJU-28⊃CsPbX<sub>3</sub> crystals with a controllable halide composition.

Various methods were carried out to confirm the successful *in situ* formation of CsPbX<sub>3</sub> NCs in ZJU-28. Powder X-ray diffraction (PXRD) was measured to investigate the crystal structure and phase of the ZJU-28 $\supset$ CsPbX<sub>3</sub> crystals. The XRD patterns of ZJU-28 at different synthesis stages are shown in Fig. 1a, where the XRD patterns of ZJU-28 (magenta line) and ZJU-28 $\supset$ Pb<sup>2+</sup> (purple line) match well with the simulated ones, indicating the phase purity of ZJU-28 crystals and the structure retention after the ion exchange process. After encapsulation of CsPbBr<sub>3</sub> NCs, several new diffraction peaks at around 15.2°, 21.5°, 30.4°, 37.7°, and 43.7° appear, which could be assigned to the (100), (110), (200), (211) and (220) planes of the cubic CsPbBr<sub>3</sub> (PDF#54-0752).<sup>13</sup> Moreover, these characteristic peaks shift to higher angles with the increase in chlorine content and to lower angles with the increase in iodine content, verifying the diverse halide composition of the CsPbX<sub>3</sub> NCs encapsulated in the ZJU-28 $\supset$ CsPbX<sub>3</sub> crystals.<sup>37</sup> The severely weakened and broadened diffraction peaks of ZJU-28 could be attributed to the encapsulation of CsPbX<sub>3</sub> with a larger particle size than the channel size of ZJU-28 and the flexible structure of ZJU-28.<sup>38</sup> PXRD patterns of the obtained colloidal CsPbX<sub>3</sub> NCs present similar results (Fig. S3, ESI<sup>†</sup>). X-Ray photoelectron spectroscopy (XPS) tests were implemented to determine the chemical composition of ZJU-28 $\supset$ CsPbX<sub>3</sub> crystals. XPS patterns of ZJU-28 $\supset$ CsPbClBr<sub>2</sub>, ZJU-28 $\supset$ CsPbBr<sub>3</sub>, and ZJU-28 $\supset$ CsPbBrI<sub>2</sub> all possess characteristic peaks of In 3d, C 1s and O 1s, which are attributed to ZJU-28 (Fig. S4, ESI<sup>†</sup>). XPS patterns of ZJU-28 $\supset$ CsPbClBr<sub>2</sub>, ZJU-28 $\supset$ CsPbBr<sub>3</sub>, and ZJU-28 $\supset$ CsPbBrI<sub>2</sub> all

possess characteristic peaks of In 3d, C 1s and O 1s, which are attributed to ZJU-28 (Fig. S4, ESI<sup>†</sup>). Characteristic peaks of Cs 3d (723.7 eV and 737.7 eV), Pb 4f (137.8 eV and 142.6 eV), and Br 3d (67.7 eV and 74.8 eV) indicate the existence of all constituent elements of CsPbBr<sub>3</sub> in ZJU-28 $\supset$ CsPbBr<sub>3</sub> (Fig. S6, ESI<sup>†</sup>). Furthermore, the additional peaks of Cl 2p (197.3 eV and 198.9 eV) for ZJU-28 $\supset$ CsPbClBr<sub>2</sub> and these of I 3d (618.3 eV and 629.7 eV) for ZJU-28 $\supset$ CsPbBrI<sub>2</sub> reveal a mixed-halide composition (Fig. S5 and S7, ESI<sup>†</sup>). Scanning electron microscopy (SEM) tests show that pristine ZJU-28 and ZJU-28 $\supset$ Pb<sup>2+</sup> crystals exhibit a topical morphology of a triangular prism with a smooth and clean surface, and the ZJU-28 $\supset$ CsPbX<sub>3</sub> crystals maintain a triangular prism shape without any perovskite crystallites on the surface of the ZJU-28 crystals, possibly resulting from the formation of CsPbX<sub>3</sub> NCs inside the ZJU-28 crystals (Fig. S8, ESI<sup>†</sup>). The elemental mapping of the ZJU-28 $\supset$ Pb<sup>2+</sup> and ZJU-28 $\supset$ CsPbX<sub>3</sub> crystals was further performed to investigate the element distribution. Fig. S9 (ESI<sup>†</sup>) shows that lead ions are uniformly distributed in ZJU-28 after the ion exchange process. After *in situ* formation of CsPbX<sub>3</sub> NCs, taking ZJU-28 $\supset$ CsPbClBr<sub>2</sub> as an example, characteristic elements such as caesium, lead, chlorine and bromine are evenly distributed in the whole selected area of the ZJU-28 single crystal (Fig. 1b). Similar results are also obtained for other samples (Fig. S10–S15, ESI<sup>†</sup>). Moreover, although the atomic ratios of caesium, lead and halogen are deviated from 1 : 1 : 3 due to the anionic frameworks of ZJU-28, the atomic ratio of different halogens matches well with the halide stoichiometry of the

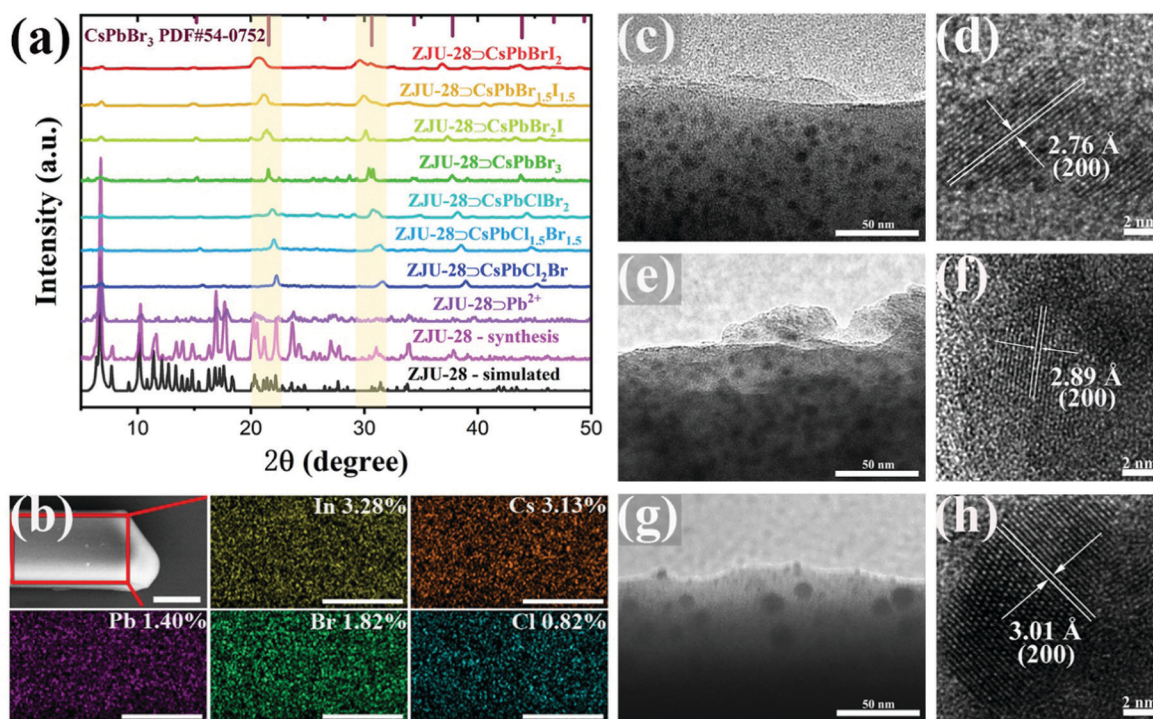


Fig. 1 (a) PXRD patterns of ZJU-28, ZJU-28 $\supset$ Pb<sup>2+</sup> and ZJU-28 $\supset$ CsPbX<sub>3</sub> crystals. (b) The SEM image of ZJU-28 $\supset$ CsPbClBr<sub>2</sub> and the corresponding elemental mapping diagrams of In, Cs, Pb, Cl, and Br. Scale bar, 5  $\mu$ m. TEM image and HR-TEM image of (c and d) ZJU-28 $\supset$ CsPbClBr<sub>2</sub>, (e and f) ZJU-28 $\supset$ CsPbBr<sub>3</sub> and (g and h) ZJU-28 $\supset$ CsPbBrI<sub>2</sub>.

CsPbX<sub>3</sub>. As shown in Fig. 1b, the atomic ratio of chlorine to bromine for ZJU-28 $\supset$ CsPbClBr<sub>2</sub> is 0.82:1.82 and very close to the corresponding stoichiometric ratio of 1:2, validating the successful regulation of the halide composition of the inner CsPbX<sub>3</sub> NCs. Transmission electron microscopy (TEM) measurements were carried out, in which uniformly distributed, monodispersed and nearly spherical particles can be directly and clearly observed in the thin edge of ZJU-28 $\supset$ CsPbClBr<sub>2</sub>, ZJU-28 $\supset$ CsPbBr<sub>3</sub>, and ZJU-28 $\supset$ CsPbBrI<sub>2</sub> crystals (Fig. 1c, e and g). High-resolution TEM tests were used to determine the observed particles. Fig. 1d, f and h clearly present the lattice fringes of these particles with interplanar distances of 2.76 Å, 2.89 Å and 3.01 Å, which can be identified as the (200) planes of cubic CsPbClBr<sub>2</sub>, CsPbBr<sub>3</sub> and CsPbBrI<sub>2</sub> respectively. The shape of the observed CsPbX<sub>3</sub> NCs in ZJU-28 $\supset$ CsPbX<sub>3</sub> is different to that of colloidal CsPbX<sub>3</sub> NCs, which could be attributed to the confinement of ZJU-28 frameworks (Fig. S17, ESI<sup>†</sup>). Furthermore, the average particle sizes of the CsPbClBr<sub>2</sub> NCs, CsPbBr<sub>3</sub> NCs and CsPbBrI<sub>2</sub> NCs encapsulated in ZJU-28 are 8.33 nm, 9.09 nm and 12.2 nm respectively, which are very close to those of the corresponding colloidal perovskite nanocrystals (9.20 nm for CsPbClBr<sub>2</sub> NCs, 9.27 nm for CsPbBr<sub>3</sub> NCs and 11.5 nm for CsPbBrI<sub>2</sub> NCs) (Fig. S16 and S17, ESI<sup>†</sup>). All the above results strongly confirm that CsPbX<sub>3</sub> NCs are successfully and uniformly *in situ* encapsulated in ZJU-28 crystals and their halide composition can be tuned easily.

Successfully encapsulating CsPbX<sub>3</sub> NCs into ZJU-28 endows ZJU-28 $\supset$ CsPbX<sub>3</sub> crystals with unique optical properties. Fig. S18 (ESI<sup>†</sup>) shows that an isolated ZJU-28 microcrystal emits violet-blue light centered at 415 nm under 365 nm excitation and maintains a similar emission (centered at 418 nm) after ion exchange with Pb<sup>2+</sup>. After encapsulation of CsPbX<sub>3</sub> NCs, ZJU-28 $\supset$ CsPbX<sub>3</sub> crystals exhibit obviously changed color and luminescence. Fig. 2d and h

show that the ZJU-28 $\supset$ CsPbBr<sub>3</sub> microcrystal emits bright green light centered at 515 nm with the full width at half maximum (FWHM) of 22.3 nm under 365 nm excitation. In the case of gradually replacing Br with Cl, microcrystals of ZJU-28 $\supset$ CsPbClBr<sub>2</sub>, ZJU-28 $\supset$ CsPbCl<sub>1.5</sub>Br<sub>1.5</sub> and ZJU-28 $\supset$ CsPbCl<sub>2</sub>Br exhibit gradually blue-shifted emission from cyan luminescence (centered at 491 nm) to blue luminescence (centered at 470 nm) and then to dark blue luminescence (centered at 450 nm), of which the corresponding FWHM is 25.7 nm, 31.3 nm and 21.3 nm, respectively (Fig. 2a–c and h). Conversely, in the case of gradually replacing Br with I, microcrystals of ZJU-28 $\supset$ CsPbBr<sub>2</sub>I, ZJU-28 $\supset$ CsPbBr<sub>1.5</sub>I<sub>1.5</sub> and ZJU-28 $\supset$ CsPbBrI<sub>2</sub> display gradually bathochromic-shifted emission from yellow-green luminescence (centered at 542 nm) to orange luminescence (centered at 593 nm) and then to red luminescence (centered at 661 nm), of which the corresponding FWHM is 25 nm, 34.5 nm and 35.4 nm, respectively (Fig. 2e–g and h). Therefore, ZJU-28 $\supset$ CsPbX<sub>3</sub> crystals exhibit halide composition-dependent emission and their emission can be tuned to cover almost the full visible spectrum.<sup>13,37</sup> Moreover, almost the entire ZJU-28 $\supset$ CsPbX<sub>3</sub> microcrystals emit bright light, confirming the uniform formation of CsPbX<sub>3</sub> NCs within ZJU-28 crystals. Fig. S19 (ESI<sup>†</sup>) shows the absorption spectra of ZJU-28 $\supset$ CsPbX<sub>3</sub> crystals, in which the lowest absorption of ZJU-28 $\supset$ CsPbX<sub>3</sub> crystals feature a similar evolution trend to their emission with the change in halide composition. It is worth mentioning that both the emission and absorption characteristics of ZJU-28 $\supset$ CsPbX<sub>3</sub> crystals are close to these of the synthesized colloidal CsPbX<sub>3</sub> NCs, indicating that the main luminescent centre of ZJU-28 $\supset$ CsPbX<sub>3</sub> is the internal CsPbX<sub>3</sub> NCs (Fig. S20 and Table S1, ESI<sup>†</sup>). The overlaps of the absorbance of CsPbX<sub>3</sub> NCs and the emission of ZJU-28 give rise to the possibility of energy transfer between each other and cause the disappearance of the

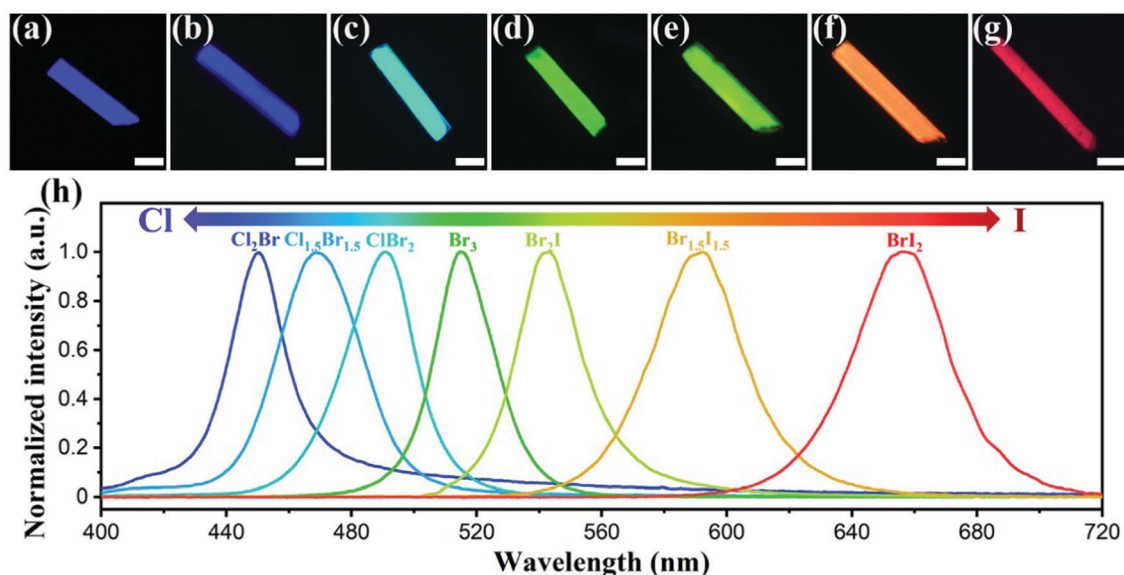


Fig. 2 The optical images of an isolated (a) ZJU-28 $\supset$ CsPbCl<sub>2</sub>Br, (b) ZJU-28 $\supset$ CsPbCl<sub>1.5</sub>Br<sub>1.5</sub>, (c) ZJU-28 $\supset$ CsPbClBr<sub>2</sub>, (d) ZJU-28 $\supset$ CsPbBr<sub>3</sub>, (e) ZJU-28 $\supset$ CsPbBr<sub>2</sub>I, (f) ZJU-28 $\supset$ CsPbBr<sub>1.5</sub>I<sub>1.5</sub> and (g) ZJU-28 $\supset$ CsPbBrI<sub>2</sub> microcrystals under excitation of 365 nm (for a–d) or 480 nm (for e–g). Scale bar, 50  $\mu$ m. (h) PL spectra of the ZJU-28 $\supset$ CsPbX<sub>3</sub> crystals.

characteristic emission of the later.<sup>39</sup> The shortened life time of the characteristic emission of the ZJU-28 (centered at around 415 nm) is further evidence for the possible energy transfer (Fig. S21, ESI†). The quantum yields of ZJU-28  $\supset$  CsPbX<sub>3</sub> crystals range from 2.45% to 27.0%, which are lower than these of colloidal CsPbX<sub>3</sub> NCs. The lower quantum yields could be attributed to different sample states during tests and no organic ligands capping on the surface of the CsPbX<sub>3</sub> NCs encapsulated in ZJU-28. More details about the optical properties of ZJU-28  $\supset$  CsPbX<sub>3</sub> crystals and colloidal CsPbX<sub>3</sub> NCs are listed in Table S1 (ESI†). It is found that encapsulation of CsPbX<sub>3</sub> NCs endows ZJU-28  $\supset$  CsPbX<sub>3</sub> crystals with the optical properties of CsPbX<sub>3</sub> NCs, which are similar to these of the colloidal counterparts, and tunable 1PE emission covering almost the whole visible region is achieved by simply adjusting the halide stoichiometry of CsX.

The two-photon excited (2PE) luminescence properties of the ZJU-28  $\supset$  CsPbX<sub>3</sub> crystals were investigated under femto-second (fs) pulsed laser excitation with a home-built system (Fig. S22, ESI†). ZJU-28  $\supset$  CsPbCl<sub>x</sub>Br<sub>3-x</sub> ( $x = 0, 1, 1.5, 2$ ) crystals were excited at 780 nm and ZJU-28  $\supset$  CsPbBr<sub>3-y</sub>I<sub>y</sub> ( $y = 1, 1.5, 2$ ) crystals were excited at 980 nm under conditions of 25 °C and 55% humidity. Fig. 3a shows that the intensity of the 2PE luminescence for all ZJU-28  $\supset$  CsPbX<sub>3</sub> crystals gradually increases without accompanying the obvious emission peak shift and split as the pump energy density increases. Fig. 3b shows that the plots of the logarithm of the emission intensity and the logarithm of the pump energy density display a linear relationship for the ZJU-28  $\supset$  CsPbX<sub>3</sub> crystals. The slopes of the fitting lines for X<sub>3</sub> = Cl<sub>2</sub>Br, Cl<sub>1.5</sub>Br<sub>1.5</sub>, ClBr<sub>2</sub>, Br<sub>3</sub>, Br<sub>2</sub>I, Br<sub>1.5</sub>I<sub>1.5</sub> and BrI<sub>2</sub> are 1.96, 1.98, 1.96, 1.95, 2.01, 2.01 and 1.99 respectively, which are all close to 2 and verify the 2PE luminescence process.<sup>38</sup> The emission color of the ZJU-28  $\supset$  CsPbX<sub>3</sub> crystals under infrared fs pulsed laser excitation is the same as these under excitation of 365 nm or 480 nm and the peak position of the 2PE luminescence is very close to that of the 1PE luminescence (Fig. 2a–h and 3a). Therefore, the 2PE luminescence of the ZJU-28  $\supset$  CsPbX<sub>3</sub> crystals is also halide composition-dependent and can be tuned to cover almost the full visible

spectrum. Moreover, the required minimum pump energy density to generate 2PE luminescence for ZJU-28  $\supset$  CsPbX<sub>3</sub> is different, which could be attributed to their composition-dependent two-photon absorption (2PA) (Fig. S23–S29, ESI†).<sup>40,41</sup> The two-photon action cross-section ( $\eta\sigma_2$ , that is, the product of photoluminescence quantum yield ( $\eta$ ) and 2PA cross-section ( $\sigma_2$ )) and the 2PE luminescence reference method were chosen to evaluate the 2PE luminescence and quantitatively determine the  $\eta\sigma_2$ , respectively (see the ESI†).<sup>38,42</sup> According to the previous reports,<sup>43</sup> the  $\eta\sigma_2$  of the ZJU-28  $\supset$  CsPbX<sub>3</sub> crystals can be calculated from the ratio of 2PE luminescence intensity (eqn (1), ESI†):

$$\eta_s\sigma_{2s} = \left(\frac{A_s}{A_{\text{ref}}}\right) \left(\frac{c_{\text{ref}}}{c_s}\right) \eta_{\text{ref}}\sigma_{2\text{ref}} \quad (1)$$

where ( $A_s/A_{\text{ref}}$ ) represents the ratio of the integral area of the 2PE luminescence band of the test sample and reference, and ( $c_{\text{ref}}/c_s$ ) represents the ratio of the molar concentration of the reference and test sample. Standard dyes, Coumarin 153, Rhodamine 6G and Rhodamine B, are chosen as the references for the ZJU-28  $\supset$  CsPbClBr<sub>2</sub>, ZJU-28  $\supset$  CsPbBr<sub>3</sub> and ZJU-28  $\supset$  CsPbBrI<sub>2</sub> crystals respectively, because the wavelength-dependent 2PA cross-section of these dyes is precisely known and their emission peak position is close to those of the corresponding samples.<sup>44</sup> More details about the samples and reference dyes are described in the ESI.† Fig. S30–S32 (ESI†) shows the 2PE luminescence comparison of the ZJU-28  $\supset$  CsPbClBr<sub>2</sub>, ZJU-28  $\supset$  CsPbBr<sub>3</sub> and ZJU-28  $\supset$  CsPbBrI<sub>2</sub> crystals with their corresponding reference dyes and colloidal perovskite NCs under the same single pulse excitation fluence respectively, from which ( $A_s/A_{\text{ref}}$ ) of the ZJU-28  $\supset$  CsPbX<sub>3</sub> crystals to the reference dyes and colloidal perovskite NCs to the reference dyes can be calculated. Therefore, the  $\eta\sigma_2$  of the ZJU-28  $\supset$  CsPbClBr<sub>2</sub>, ZJU-28  $\supset$  CsPbBr<sub>3</sub> and ZJU-28  $\supset$  CsPbBrI<sub>2</sub> crystals was calculated to be  $8.66 \times 10^4$  GM (780 nm excitation),  $1.58 \times 10^6$  GM (780 nm excitation) and  $1.96 \times 10^5$  GM (980 nm excitation), respectively. Meanwhile, the  $\eta\sigma_2$  of colloidal CsPbClBr<sub>2</sub> NCs, CsPbBr<sub>3</sub> NCs and CsPbBrI<sub>2</sub> NCs was also calculated to be  $8.93 \times 10^4$  GM (780 nm excitation),  $1.45 \times 10^6$  GM (780 nm excitation) and  $2.43 \times 10^5$  GM (980 nm excitation) respectively, which are consistent with the previous reports (Table S2, ESI†).<sup>7,8,40</sup>



Fig. 3 (a) Two-photon excited luminescence of the ZJU-28  $\supset$  CsPbX<sub>3</sub> crystals under fs pulsed laser excitation at 780 nm (for X<sub>3</sub> = Cl<sub>2</sub>Br, Cl<sub>1.5</sub>Br<sub>1.5</sub>, ClBr<sub>2</sub> and Br<sub>3</sub>) or 980 nm (for X<sub>3</sub> = Br<sub>2</sub>I, Br<sub>1.5</sub>I<sub>1.5</sub> and BrI<sub>2</sub>). Insets: The microscopy images of ZJU-28  $\supset$  CsPbX<sub>3</sub> crystals upon infrared fs pulsed laser excitation. Scale bar, 50  $\mu$ m. (b) Pump energy density-dependent 2PE emission intensity of the ZJU-28  $\supset$  CsPbX<sub>3</sub> crystals. The inset displays the slopes of the logarithm of the emission intensity and the logarithm of the pump energy. Test environment: temperature of 25 °C, humidity of 55%.

Obviously, ZJU-28 $\supset$ CsPbX<sub>3</sub> crystals possess giant  $\eta\sigma_2$ , comparable to those of colloidal CsPbX<sub>3</sub> NCs dispersed in toluene. Considering that the high nonlinear absorption capacity of NCs is primarily derived from their strong dielectric confinement and surface enhancement effects,<sup>45,46</sup> and no organic ligands bind to the surface of the CsPbX<sub>3</sub> NCs encapsulated in the ZJU-28 crystals, therefore, the giant two-photon action cross-sections of the ZJU-28 $\supset$ CsPbX<sub>3</sub> crystals could be mainly attributed to confinement and surface passivation of the ZJU-28 frameworks.<sup>38,42</sup>

In order to meet the urgent requirements of the stability improvement of perovskite NCs in practical applications, the photostability of ZJU-28 $\supset$ CsPbX<sub>3</sub> crystals and colloidal CsPbX<sub>3</sub> NCs (for the comparison) was mainly studied under 25 °C and 55% humidity. For the 1PE photostability tests, ZJU-28 $\supset$ CsPbX<sub>3</sub> crystals were continuously illuminated at 365 nm or 480 nm, of which the corresponding power densities are 598 mW cm<sup>-2</sup> and 336 mW cm<sup>-2</sup>, respectively. Fig. S33 (ESI<sup>†</sup>) shows the plots of the relative PL intensity of the ZJU-28 $\supset$ CsPbX<sub>3</sub> crystals and the corresponding colloidal CsPbX<sub>3</sub> NCs as a function of irradiation time, in which about 79.9%, 90.7%, 75.1%, 80.7%, 78.2%, 66.5% and 28.5% of the initial

luminescence intensity were preserved after 90 min of irradiation for ZJU-28 $\supset$ CsPbCl<sub>2</sub>Br, ZJU-28 $\supset$ CsPbCl<sub>1.5</sub>Br<sub>1.5</sub>, ZJU-28 $\supset$ CsPbClBr<sub>2</sub>, ZJU-28 $\supset$ CsPbBr<sub>3</sub>, ZJU-28 $\supset$ CsPbBr<sub>2</sub>I, ZJU-28 $\supset$ CsPbBr<sub>1.5</sub>I<sub>1.5</sub> and ZJU-28 $\supset$ CsPbBrI<sub>2</sub>, respectively. However, the luminescence intensity of colloidal CsPbX<sub>3</sub> NCs dropped much faster especially when the solvent volatilized completely and there was no obvious luminescence after no more than 30 min irradiation. These results indicate that encapsulating CsPbX<sub>3</sub> NCs into ZJU-28 crystals provides significant enhancement of 1PE photostability. As for colloidal CsPbX<sub>3</sub> NCs, the nanocrystals are densely in contact with each other after the solvent evaporated completely and light-induced regrowth and deterioration might occur due to the dynamic bounding of the surface ligands to CsPbX<sub>3</sub> NCs.<sup>47</sup> In contrast, the ZJU-28 frameworks effectively separate the CsPbX<sub>3</sub> NCs and make them monodispersed in ZJU-28 $\supset$ CsPbX<sub>3</sub> crystals (Fig. 1c, e and g). We speculate that this isolation effect is one reason for the enhancement of the photostability.<sup>22</sup> In addition, time-resolved PL decays of ZJU-28 $\supset$ CsPbX<sub>3</sub> crystals and colloidal CsPbX<sub>3</sub> NCs were measured (Fig. S34, ESI<sup>†</sup>) and fitted by a biexponential decay function. The slower component  $\tau_2$ , which is attributed to

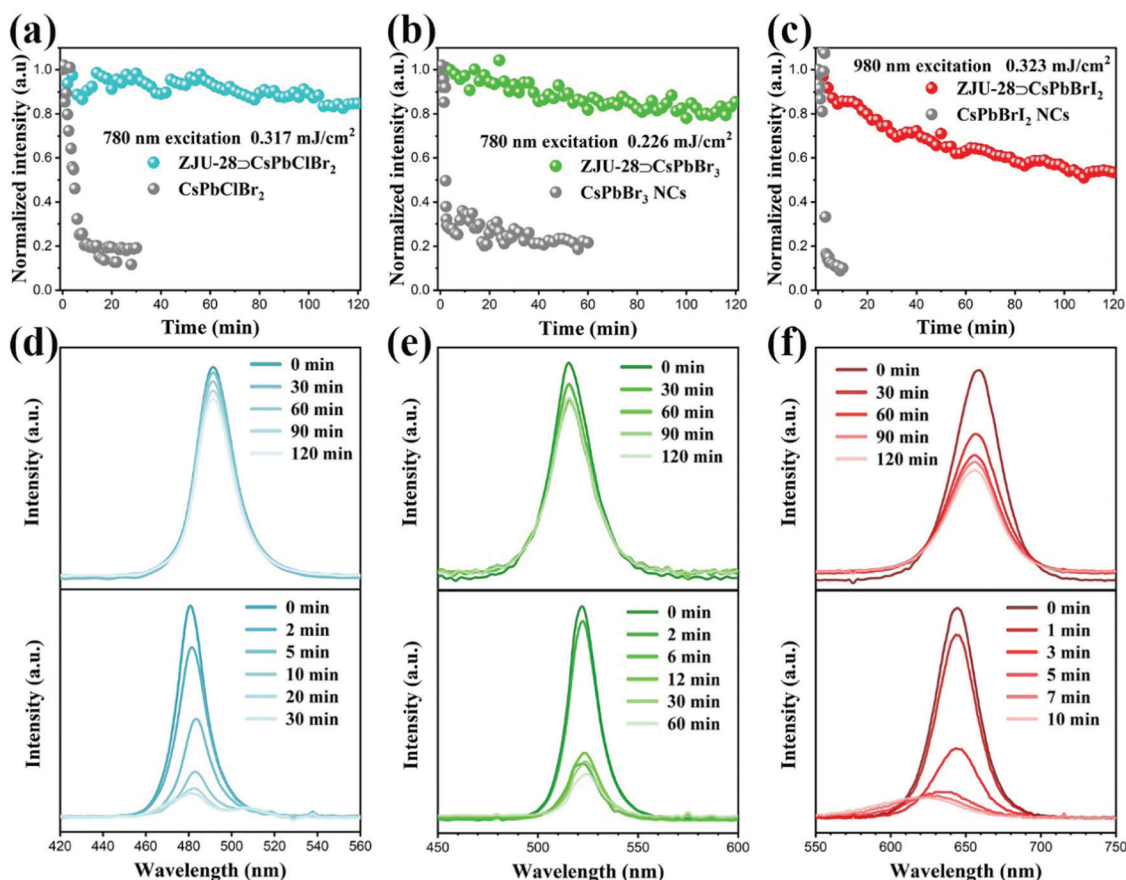


Fig. 4 Plots of relative 2PE luminescence intensity of an isolated (a) ZJU-28 $\supset$ CsPbClBr<sub>2</sub>, (b) ZJU-28 $\supset$ CsPbBr<sub>3</sub> and (c) ZJU-28 $\supset$ CsPbBrI<sub>2</sub> microcrystal with corresponding perovskite NCs under fs laser excitation as a function of irradiation time. (d) PL spectra changes of an isolated ZJU-28 $\supset$ CsPbClBr<sub>2</sub> microcrystal (top) and CsPbClBr<sub>2</sub> NCs (below) under 780 nm excitation for different time periods. (e) PL spectra changes of an isolated ZJU-28 $\supset$ CsPbBr<sub>3</sub> microcrystal (top) and CsPbBr<sub>3</sub> NCs (below) under 780 nm excitation for different time periods. (f) PL spectra changes of an isolated ZJU-28 $\supset$ CsPbBrI<sub>2</sub> microcrystal (top) and CsPbBrI<sub>2</sub> NCs (below) under 980 nm excitation for different time periods. Test environment: temperature of 25 °C, humidity of 55%.

surface trap assisted recombination, is longer in the ZJU-28  $\supset$  CsPbX<sub>3</sub> crystals than in colloidal CsPbX<sub>3</sub> NCs, indicating effective surface passivation derived from ZJU-28 frameworks.<sup>48</sup> This effective surface passivation could be another reason for the improvement of photostability. Furthermore, after storing in the air without additional protection for 6 months, ZJU-28  $\supset$  CsPbBr<sub>3</sub> crystals still exhibit bright green emission upon excitation, and maintain around 78% of the initial emission intensity after 90 min irradiation at 365 nm with the power density of 598 mW cm<sup>-2</sup> (Fig. S35, ESI<sup>†</sup>), indicating the excellent long-term stability of the ZJU-28  $\supset$  CsPbX<sub>3</sub> crystals.

The 2PE photostability of ZJU-28  $\supset$  CsPbX<sub>3</sub> crystals was investigated upon fs laser excitation at 780 nm (for X<sub>3</sub> = Cl<sub>2</sub>Br, Cl<sub>1.5</sub>Br<sub>1.5</sub>, ClBr<sub>2</sub> and Br<sub>3</sub>) and 980 nm (for X<sub>3</sub> = Br<sub>2</sub>I, Br<sub>1.5</sub>I<sub>1.5</sub> and BrI<sub>2</sub>) under 25 °C and 55% humidity. Fig. 4 shows the illumination-time-dependent 2PE luminescence intensity of ZJU-28  $\supset$  CsPbClBr<sub>2</sub>, ZJU-28  $\supset$  CsPbBr<sub>3</sub> and ZJU-28  $\supset$  CsPbBrI<sub>2</sub> crystals upon infrared fs laser excitation, which clearly displays a much slower drop than the corresponding colloidal CsPbX<sub>3</sub> NCs. Therein, about 83.3% and 20% of the initial luminescence intensity was maintained for ZJU-28  $\supset$  CsPbBr<sub>3</sub> and CsPbBr<sub>3</sub> NCs respectively after 120 min irradiation of 780 nm (0.226 mJ cm<sup>-2</sup>) (Fig. 4b) and there was no emission peak shift and split under continuous irradiation for both (Fig. 4e). The ZJU-28  $\supset$  CsPbClBr<sub>2</sub> crystals kept about 85.1% of the initial luminescence intensity after 120 min irradiation of 780 nm (0.317 mJ cm<sup>-2</sup>), which was much higher than that of CsPbClBr<sub>2</sub> NCs (about 18.7%) (Fig. 4a). During continuous irradiation, ZJU-28  $\supset$  CsPbClBr<sub>2</sub> crystals still presented no obvious peak shift and split but there was a new emission peak centered at around 506 nm for the CsPbClBr<sub>2</sub> NCs (Fig. 4d). Similarly, new emission peaks centered at 415 nm and 484 nm for CsPbCl<sub>2</sub>Br NCs and CsPbCl<sub>1.5</sub>Br<sub>1.5</sub> NCs appeared respectively but no emission peak split was observed for ZJU-28  $\supset$  CsPbCl<sub>2</sub>Br and ZJU-28  $\supset$  CsPbCl<sub>1.5</sub>Br<sub>1.5</sub> crystals under continuous irradiation (Fig. S36 and S37, ESI<sup>†</sup>). ZJU-28  $\supset$  CsPbBrI<sub>2</sub> crystals held 53.5% of the initial luminescence intensity after 120 min irradiation of the 980 nm fs laser with a single pulse energy density of 0.323 mJ cm<sup>-2</sup> but CsPbBrI<sub>2</sub> NCs only preserved around 10% after 10 min irradiation under the same conditions (Fig. 4c). In addition, the emission peak of the CsPbBrI<sub>2</sub> NCs shifted significantly from 644 nm to 619 nm but no obvious emission peak shift was observed for ZJU-28  $\supset$  CsPbBrI<sub>2</sub> crystals upon continuous excitation of the 980 nm fs laser (Fig. 4f). Fig. S38 and S39 (ESI<sup>†</sup>) also show that CsPbBr<sub>2</sub>I NCs and CsPbBr<sub>1.5</sub>I<sub>1.5</sub> NCs have experienced an obvious emission peak shift while ZJU-28  $\supset$  CsPbBr<sub>2</sub>I and ZJU-28  $\supset$  CsPbBr<sub>1.5</sub>I<sub>1.5</sub> crystals have no emission peak shift under continuous irradiation. Besides greatly slowed attenuation of the 2PE luminescence intensity, ZJU-28  $\supset$  CsPbX<sub>3</sub> crystals also exhibit stable emission characteristics without any emission peak split and shift under continuous irradiation of an infrared fs pulse laser. We speculate that this emission peak split and shift of the mixed-halide perovskite NCs can be imputed to the light-induced ion segregation and phase separation.<sup>19,20</sup> ZJU-28 frameworks can isolate the internal CsPbX<sub>3</sub> NCs and passivate their surface defects, thus allowing them to retain their original size and a highly stable homogenous phase.<sup>49,50</sup> Therefore,

confinement of CsPbX<sub>3</sub> NCs in the ZJU-28 crystals leads to enhancement of 2PE spectral stability and photostability.

Apart from the photostability, the thermal and water stability of the ZJU-28  $\supset$  CsPbX<sub>3</sub> crystals were also tested. Fig. S40 (ESI<sup>†</sup>) shows the thermal stability test of ZJU-28  $\supset$  CsPbClBr<sub>2</sub>, ZJU-28  $\supset$  CsPbBr<sub>3</sub> and ZJU-28  $\supset$  CsPbBrI<sub>2</sub> crystals and their PL intensity monotonically decreases as the temperature rises. ZJU-28  $\supset$  CsPbBr<sub>3</sub> crystals present the best thermal stability and still maintain half of the initial luminous intensity up to 80 °C. Despite the inferior thermal stability of the ZJU-28  $\supset$  CsPbClBr<sub>2</sub> and ZJU-28  $\supset$  CsPbBrI<sub>2</sub> crystals, their emission peak remains constant with temperature changes, which indicates the composition stability at different temperatures. It is known that lead halide perovskites are very sensitive to water and degrade fast in water. Surprisingly, after immersion in water for 2 hour, ZJU-28  $\supset$  CsPbBr<sub>3</sub> crystals still emit bright green light and about half of the initial PL intensity was maintained, which confirms their excellent water stability (Fig. S41, ESI<sup>†</sup>).

Combined with a highly tunable, narrow emission and significantly enhanced photostability, ZJU-28  $\supset$  CsPbX<sub>3</sub> crystals exhibit great potential in backlight displays. A facile LED device was constructed by combining a UV chip, ZJU-28  $\supset$  CsPbBr<sub>3</sub> crystals and ZJU-28  $\supset$  CsPbBrI<sub>2</sub> crystals. As shown in Fig. S42 (ESI<sup>†</sup>), the fabricated LED device presents a mixed output of red, green and blue light with corresponding color coordinates of (0.330, 0.347), which is very close to (0.33, 0.33). In addition, due to the pure color emission of ZJU-28  $\supset$  CsPbX<sub>3</sub> crystals, the color gamut of the fabricated device covers almost 112% of the NTSC standard.<sup>51</sup>

## Conclusions

In summary, the host-guest ZJU-28  $\supset$  CsPbX<sub>3</sub> was successfully constructed by encapsulating CsPbX<sub>3</sub> NCs in ZJU-28 crystals *via* the sequential deposition method, during which the composition of the *in situ* encapsulated CsPbX<sub>3</sub> NCs can be precisely tuned by simply adjusting the halide stoichiometry of CsX. The encapsulation of CsPbX<sub>3</sub> NCs and adjustment of their halide composition can be realized in ambient conditions owing to the unique features of MOFs. The 1PE and 2PE emission of the acquired ZJU-28  $\supset$  CsPbX<sub>3</sub> crystals can be modulated from 450 nm to 661 nm, which covers almost the whole visible region. Importantly, the confinement and surface passivation of CsPbX<sub>3</sub> NCs derived from ZJU-28 frameworks endow ZJU-28  $\supset$  CsPbX<sub>3</sub> crystals with giant  $\eta_{\sigma_2}$ . The values of  $\eta_{\sigma_2}$  for ZJU-28  $\supset$  CsPbClBr<sub>2</sub> (at 780 nm), ZJU-28  $\supset$  CsPbBr<sub>3</sub> (at 780 nm) and ZJU-28  $\supset$  CsPbBrI<sub>2</sub> (at 980 nm) were calculated to be  $8.66 \times 10^4$  GM,  $1.58 \times 10^6$  GM and  $1.96 \times 10^5$  GM respectively, which is comparable to those of colloidal CsPbX<sub>3</sub> NCs dispersed in toluene. Moreover, the ZJU-28 frameworks still separate, passivate and protect the internal CsPbX<sub>3</sub> NCs, resulting in a great enhancement of 1PE and 2PE photostability for the ZJU-28  $\supset$  CsPbX<sub>3</sub> crystals. These unique, tunable and photostable ZJU-28  $\supset$  CsPbX<sub>3</sub> crystals show great potential in wide color-gamut backlight display, bioimaging, sensing and even future integrated photonics.

## Conflicts of interest

There are no conflicts to declare.

## Acknowledgements

The authors acknowledge the financial support from the National Natural Science Foundation of China (No. 52025131 and 61721005).

## Notes and references

- J. Shamsi, A. S. Urban, M. Imran, L. D. Trizio and L. Manna, *Chem. Rev.*, 2019, **119**, 3296–3348.
- F. Yan, S. T. Tan, X. Li and H. V. Demir, *Small*, 2019, **15**, 1902079.
- H. Wang and D. H. Kim, *Chem. Soc. Rev.*, 2017, **46**, 5204–5236.
- X. Wang, Z. Bao, Y.-C. Chang and R. S. Liu, *ACS Energy Lett.*, 2020, **5**, 3374–3396.
- J. Song, J. Li, X. Li, L. Xu, Y. Dong and H. Zeng, *Adv. Mater.*, 2015, **27**, 7162–7167.
- Y. Wang, X. Li, J. Song, L. Xiao, H. Zeng and H. Sun, *Adv. Mater.*, 2015, **27**, 7101–7108.
- Y. Wang, X. Li, X. Zhao, L. Xiao, H. Zeng and H. Sun, *Nano Lett.*, 2016, **16**, 448–453.
- Y. Xu, Q. Chen, C. Zhang, R. Wang, H. Wu, X. Zhang, G. Xing, W. W. Yu, X. Wang, Y. Zhang and M. Xiao, *J. Am. Chem. Soc.*, 2016, **138**, 3761–3768.
- J. Yu, Y. Cui, C. D. Wu, Y. Yang, B. Chen and G. Qian, *J. Am. Chem. Soc.*, 2015, **137**, 4026–4029.
- J. Chen, K. Židek, P. Chábera, D. Liu, P. Cheng, L. Nuuttila, M. J. Al-Marri, H. Lehtivuori, M. E. Messing, K. Han, K. Zheng and T. Pullerits, *J. Phys. Chem. Lett.*, 2017, **8**, 2316–2321.
- T. He, J. Li, X. Qiu, S. Xiao, C. Yin and X. Lin, *Adv. Opt. Mater.*, 2018, **6**, 1800843.
- A. Pramanik, K. Gates, Y. Gao, S. Begum and P. Chandra Ray, *J. Phys. Chem. C*, 2019, **123**, 5150–5156.
- L. Protesescu, S. Yakunin, M. I. Bodnarchuk, F. Krieg, R. Caputo, C. H. Hendon, R. X. Yang, A. Walsh and M. V. Kovalenko, *Nano Lett.*, 2015, **15**, 3692–3696.
- F. Zhao, J. Li, X. Gao, X. Qiu, X. Lin, T. He and R. Chen, *J. Phys. Chem. C*, 2019, **123**, 9538–9543.
- Y. Wei, Z. Cheng and J. Lin, *Chem. Soc. Rev.*, 2019, **48**, 310–350.
- Y. Lin, X. Zheng, Z. Shangguan, G. Chen, W. Huang, W. Guo, X. Fan, X. Yang, Z. Zhao, T. Wu and Z. Chen, *J. Mater. Chem. C*, 2021, **9**, 12303–12313.
- Q. Zhang, Y. Zhou, Y. Wei, M. Tai, H. Nan, Y. Gu, J. Han, X. Yin, J. Li and H. Lin, *J. Mater. Chem. C*, 2020, **8**, 2569–2578.
- Q. Zhang, H. Nan, Y. Zhou, Y. Gu, M. Tai, Y. Wei, F. Hao, J. Li, D. Oron and H. Lin, *J. Mater. Chem. C*, 2019, **7**, 6795–6804.
- H. Zhang, X. Fu, Y. Tang, H. Wang, C. Zhang, W. W. Yu, X. Wang, Y. Zhang and M. Xiao, *Nat. Commun.*, 2019, **10**, 1088.
- P. Vashishtha and J. E. Halpert, *Chem. Mater.*, 2017, **29**, 5965–5973.
- Y. Hassan, J. H. Park, M. L. Crawford, A. Sadhanala, J. Lee, J. C. Sadighian, E. Mosconi, R. Shivanna, E. Radicchi, M. Jeong, C. Yang, H. Choi, S. H. Park, M. H. Song, F. De Angelis, C. Y. Wong, R. H. Friend, B. R. Lee and H. J. Snaith, *Nature*, 2021, **591**, 72–77.
- X. Li, Y. Wang, H. Sun and H. Zeng, *Adv. Mater.*, 2017, **29**, 1701185.
- Y. J. Yoon, Y. Chang, S. Zhang, M. Zhang, S. Pan, Y. He, C. H. Lin, S. Yu, Y. Chen, Z. Wang, Y. Ding, J. Jung, N. Thadhani, V. V. Tsukruk, Z. Kang and Z. Lin, *Adv. Mater.*, 2019, **31**, 1901602.
- D. N. Dirin, B. M. Benin, S. Yakunin, F. Krumeich, G. Raino, R. Frison and M. V. Kovalenko, *ACS Nano*, 2019, **13**, 11642–11652.
- X. Liang, M. Chen, Q. Wang, S. Guo and H. Yang, *Angew. Chem., Int. Ed.*, 2019, **58**, 2799–2803.
- S. Yuan, D. Chen, X. Li, J. Zhong and X. Xu, *ACS Appl. Mater. Interfaces*, 2018, **10**, 18918–18926.
- R. Li, Z. Wei, H. Zhao, H. Yu, X. Fang, D. Fang, J. Li, T. He, R. Chen and X. Wang, *Nanoscale*, 2018, **10**, 22766–22774.
- H. Zhang, M. Jin, X. Liu, Y. Zhang, Y. Yu, X. Liang, W. Xiang and T. Wang, *Nanoscale*, 2019, **11**, 18009–18014.
- Y. Tong, Q. Wang, E. Mei, X. Liang, W. Gao and W. Xiang, *Adv. Opt. Mater.*, 2021, **9**, 2100012.
- Y. Cui, J. Zhang, H. He and G. Qian, *Chem. Soc. Rev.*, 2018, **47**, 5740–5785.
- H. He, E. Ma, Y. Cui, J. Yu, Y. Yang, T. Song, C. D. Wu, X. Chen, B. Chen and G. Qian, *Nat. Commun.*, 2016, **7**, 11087.
- Z. G. Gu, D. J. Li, C. Zheng, Y. Kang, C. Woll and J. Zhang, *Angew. Chem., Int. Ed.*, 2017, **56**, 6853–6858.
- Z. Yuan, L. Zhang, S. Li, W. Zhang, M. Lu, Y. Pan, X. Xie, L. Huang and W. Huang, *J. Am. Chem. Soc.*, 2018, **140**, 15507–15515.
- S. K. Yadav, G. K. Grandhi, D. P. Dubal, J. C. de Mello, M. Otyepka, R. Zboril, R. A. Fischer and K. Jayaramulu, *Small*, 2020, **16**, 2004891.
- C. Zhang, W. Li and L. Li, *Angew. Chem., Int. Ed.*, 2021, **60**, 7488–7501.
- J. Yu, Y. Cui, C. Wu, Y. Yang, Z. Wang, M. O’Keeffe, B. Chen and G. Qian, *Angew. Chem., Int. Ed.*, 2012, **51**, 10542–10545.
- Q. A. Akkerman, V. D’Innocenzo, S. Accornero, A. Scarpellini, A. Petrozza, M. Prato and L. Manna, *J. Am. Chem. Soc.*, 2015, **137**, 10276–10281.
- H. He, Y. Cui, B. Li, B. Wang, C. Jin, J. Yu, L. Yao, Y. Yang, B. Chen and G. Qian, *Adv. Mater.*, 2019, **31**, 1806897.
- S. Bhattacharyya, D. Rambabu and T. K. Maji, *J. Mater. Chem. A*, 2019, **7**, 21106–21111.
- W. Chen, F. Zhang, C. Wang, M. Jia, X. Zhao, Z. Liu, Y. Ge, Y. Zhang and H. Zhang, *Adv. Mater.*, 2021, **33**, 2004446.
- J. Xu, X. Li, J. Xiong, C. Yuan, S. Semin, T. Rasing and X. H. Bu, *Adv. Mater.*, 2020, **32**, 1806736.



- 42 W. Chen, S. Bhaumik, S. A. Veldhuis, G. Xing, Q. Xu, M. Grätzel, S. Mhaisalkar, N. Mathews and T. C. Sum, *Nat. Commun.*, 2017, **8**, 15198.
- 43 R. Medishetty, J. K. Zareba, D. Mayer, M. Samoc and R. A. Fischer, *Chem. Soc. Rev.*, 2017, **46**, 4976–5004.
- 44 N. S. Makarov, M. Drobizhev and A. Rebane, *Opt. Express*, 2008, **16**, 4029.
- 45 H. He and T. C. Sum, *Dalton Trans.*, 2020, **49**, 15149–15160.
- 46 W. Liu, J. Xing, J. Zhao, X. Wen, K. Wang, P. Lu and Q. Xiong, *Adv. Opt. Mater.*, 2017, **5**, 1601045.
- 47 J. Chen, D. Liu, M. J. Al-Marri, L. Nuuttila, H. Lehtivuori and K. Zheng, *Sci. China Mater.*, 2016, **59**, 719–727.
- 48 S. Li, D. Lei, W. Ren, X. Guo, S. Wu, Y. Zhu, A. L. Rogach, M. Chhowalla and A. K. Y. Jen, *Nat. Commun.*, 2020, **11**, 11.
- 49 X. Wang, Y. Ling, X. Lian, Y. Xin, K. B. Dhungana, F. Perez-Orive, J. Knox, Z. Chen, Y. Zhou, D. Beery, K. Hanson, J. Shi, S. Lin and H. Gao, *Nat. Commun.*, 2020, **11**(10), 695.
- 50 A. J. Knight and L. M. Herz, *Energy Environ. Sci.*, 2020, **13**, 2024–2046.
- 51 H. C. Wang, S. Y. Lin, A. C. Tang, B. P. Singh, H. C. Tong, C. Y. Chen, Y. C. Lee, T. L. Tsai and R. S. Liu, *Angew. Chem., Int. Ed.*, 2016, **55**, 7924–7929.